Tecnociencia, Vol. 28, N°1: 238-263
Enero-Junio 2026
ISSN L 2415-0940

Parameters Characterization of Exoplanet WASP-10b Using Two Transit Surveys

Caracterización de los parámetros del exoplaneta WASP-10b mediante dos sondeos de tránsito

Franklin Simón Vásquez Guardia
Università degli Studi di Padova, Dipartimento di Fisica e Astronomia "Galileo Galilei", Italia.
franklinsimon.vasquezguardia@studenti.unipd.it https://orcid.org/0000-0002-1413-6617

Fecha de recepción: 13 de octubre de 2025
Fecha de aceptación: 20 de noviembre de 2025

DOI: https://doi.org/10.48204/j.tecno.v28n1.a8961

ABSTRACT

The transit method, with over 4000 confirmed exoplanets to date, remains one of the most prolific and robust techniques in the field. This study focuses on the WASP-10 system, a K5-type star located 92 parsecs from Earth, which hosts the confirmed exoplanet WASP-10b. We present a detailed analysis of data from the TESS and TASTE surveys to characterize the planetary parameters of WASP-10b and compare them with values reported in the literature. Although both surveys employ the transit method, their observational strategies and data reduction pipelines differ substantially. Consequently, the datasets were processed independently and subsequently analyzed using a Markov Chain Monte Carlo (MCMC) framework to determine the orbital and physical parameters that best reproduce the observed light curves.

KEYWORDS

Differential photometry, detrending, Bayesian statistics, photometric observations (TESS, TASTE), data analysis, WASP-10b.

RESUMEN

El método de detección de exoplanetas mediante tránsitos, con más de 4000 exoplanetas confirmados por esta técnica hasta la fecha, es una de las más robustas y eficientes en el campo. En este trabajo se estudia el sistema estelar WASP-10, una estrella tipo K5 situada a 92 parsecs de la Tierra, donde se ha reportado el exoplaneta

WASP-10b. Se discute el proceso de extracción y procesamiento de datos de los sondeos TESS y TASTE, realizados sobre el sistema WASP-10, para caracterizar los parámetros del exoplaneta WASP-10b y comparar los resultados con la literatura existente. Mientras que ambos sondeos emplean el método de tránsito, sus enfoques y procedimientos difieren significativamente; por ello, los datos se procesaron por separado y luego se analizaron mediante un cálculo de Markov Chain Monte Carlo (MCMC) para obtener los parámetros orbitales y planetarios más compatibles con los modelos derivados.

PALABRAS CLAVE

Fotometría diferencial, eliminación de tendencias, estadística bayesiana, observaciones fotométricas TESS y TASTE, análisis de datos, WASP-10b.

INTRODUCTION

The search for exoplanets addresses one of humanity's most fundamental questions: the existence of other worlds like our own, but among other stars. Dating back to the IVth century, Epicurus and Democritus proposed there must be other worlds aside from our own; however, no solid proof could be provided due to the technological limitations of their time. It was not until 1995 when Didier Queloz and Michel Mayor (Mayor and Queloz 1995) put forth the most convincing evidence of an exoplanet orbiting another star that a new scientific revolution began, a revolution that, in the 29 years since their discovery, has yielded an astounding number of almost 6000 exoplanets at the date of this publication.

At present, many techniques have been developed to aid in the search for exoplanets with varying configurations of equipment and requirements for different targets and goals; however, one of the most successful techniques has been the transit method, with over 4000 out of 6000 exoplanets having been first reported by this method as of this date.

The transit method consists of quantifying a star's luminosity over time and measuring dips in the luminosity of the star due to an exoplanet crossing in front of it. If an exoplanet's orbit around its host star aligns in such a way that relative to us it obscures some of the star's light, we can measure and quantify the dip in the luminosity output or flux and extrapolate certain parameters about the planet such as its size relative to the size of its host star, the inclination of the orbit, its semi-major axis relative to its host-star size, and, if more than one transit is observed, the period length can be obtained as well.

Our object of interest is the WASP-10 system, a K5 star 300 light-years away (≈ 92 pc) from Earth, where an exoplanet WASP-10b was first reported by (Christian et al. 2009). Our objective is to characterize the exoplanet parameters utilizing the transit method with data from TESS (Transiting Exoplanet Survey Satellite) and TASTE (The Asiago Search for Transit Timing Variations of Exoplanets; Nascimbeni et al. 2011) surveys and compare them with the reported literature about WASP-10b.

Both datasets allow us to estimate planetary parameters for the exoplanet candidate by extracting information from the data each survey recorded. These estimated parameters are later input into a Markov Chain Monte Carlo (MCMC) calculation to statistically obtain orbital and planetary parameters that best fit the models generated from both surveys.

The data from TESS and TASTE were processed separately since the data reduction process is different in both cases. For TASTE, the data reduction had to be done manually; that is, the acquisition of properly calibrated science frames must be performed beforehand by performing BIAS, FLAT and SCIENCE frame corrections; then differential photometry was performed on the target star as well as normalization and polynomial fitting for the light-curve model to be generated. For TESS, the data could be downloaded pre-processed, requiring only a fitting for the light curve, which is available to download directly as well.

INSTRUMENTATION

The TASTE survey data were obtained at the Asiago Astrophysical Observatory, located on Mount Ekar in northern Italy at an altitude of 1 366 m. The imaging instrument used at the 1.82 m Cassegrain telescope is the AFOSC (Asiago Faint Object Spectrograph and Camera), a focal-reducer camera equipped with a 2048 × 2048 E2V CCD that provides an 8.5′ × 8.5′ field of view, a fast read-out mode, and a quantum efficiency exceeding 90 % around the R band. The observations of WASP-10 analyzed in this work were performed during the night of 28–29 October 2022, starting at 21:07:24 UTC and ending at 01:21:20 UTC, covering approximately 4.23 h of continuous monitoring. This interval includes the complete transit event and a sufficient out-of-transit baseline for reliable normalization. The raw and calibration frames (bias, flats, and science images) were provided by the TASTE collaboration at the Asiago Astrophysical Observatory (Nascimbeni et al. 2011; TASTE Collaboration 2022).

Complementary space-based data were obtained from the Transiting Exoplanet Survey Satellite (TESS), a NASA mission operating in a highly elliptical 13.7-day orbit around Earth. TESS is designed to monitor bright G-, K-, and M-type stars for planetary transits and has, to date, confirmed more than 1,500 exoplanets. The satellite observes the sky in 27-day sectors using four identical wide-field cameras, each equipped with a 4096 × 4096 back-illuminated CCD detector and providing a 24° × 24° field of view, resulting in a combined coverage of 96° × 24° per pointing. Our dataset corresponds to Sector 56 (orbits 119–120), observed from 2022-09-02 18:07:08 UTC to 2022-09-30 15:25:39 UTC, providing 27.89 days of nearly continuous science data. This sector includes nine observed transits of the exoplanet candidate WASP-10 b.

Before assessing any analysis of our derived parameters, we first ensured that the data reduction process was performed correctly. In the following sections, we describe the procedures used to extract and process both the TASTE and TESS datasets. The data analysis was performed using Python 3.9, utilizing NumPy (Harris et al. 2020), Astropy (Astropy Collaboration 2022), and Matplotlib (Hunter 2007).

DATA PROCESSING

TASTE data reduction

The initial step in reducing the TASTE dataset was to produce calibrated science frames, where the differential photometry would be performed. To achieve this, several corrections were required beforehand.

The images obtained from modern telescopes are the result of photons passing through the optical system and being converted into an electric charge proportional to the number of photons detected by the CCD. This charge, expressed in ADU (analog-to-digital units), is proportional to the photon flux received. Since the photon flux follows a Poisson distribution, it is preferable to convert ADUs into photoelectrons (e^-) at the start of the reduction. Thus, each FITS file's pixel values were multiplied by the GAIN value specified in the header.

Bias Correction

To properly obtain useful scientific images from TASTE, several processing steps must be applied to remove all possible sources of noise. The first of these is the readout noise (RON), which is an intrinsic electronic noise generated by the current that powers the CCD electronics, particularly at the amplifier stage. This type of noise sets a physical limit on the CCD's performance, since it cannot be eliminated without turning off the electronics. To quantify and correct the signal offset introduced by this noise, we apply the BIAS frame correction.

The BIAS frame represents the baseline electronic current detected by the CCD while it is powered on but not exposed to light. Even in the absence of incoming photons, the CCD records a small number of electrons due to the operation of its electronics.

The exposure time of a BIAS frame is set to zero in order to measure only this electronic noise component. However, once the CCD is exposed to photons, additional types of noise appear, which must later be corrected through the FLAT field correction.

To correct for the electronic noise, we first created a single BIAS frame to subtract from all scientific images, thereby removing the base current from the data. This was done by computing the median of all individual BIAS frames. The median was chosen over the mean for its robustness against outliers, yielding a more reliable representation of the BIAS signal, denoted as $\tilde{B}$.

Since mathematical operations are involved in computing the median BIAS, error propagation must be considered. The associated uncertainty of a single BIAS frame can be obtained in two ways:

- From the readout noise value declared in the header of the FITS file.
- By computing the standard deviation of a single BIAS frame.

Alternatively, by approximating the median to the mean, the propagation of errors can also be computed using the standard error propagation formula:

$$\sigma_{\bar{B}} = \sqrt{\sum_{i=1}^{N} (1/N)^2 \sigma_i^2} = \frac{\sigma}{\sqrt{N}}$$

Thus, the uncertainty associated with the median BIAS can be evaluated by any of the following methods:

- Dividing the readout noise declared in the header by the square root of *N* frames.
- Computing the standard deviation of the median BIAS frame and dividing by √*N*.
- Taking the standard deviation of the median BIAS frame directly.
- Calculating the standard deviation per pixel across all frames, dividing each by √*N*, and taking the median of the resulting values.

For this study, we selected the first method, taking the readout noise from the header and dividing it by √*N*, since it yielded the lowest associated error and differed from the other methods by less than 30%. This approach effectively corrects small inhomogeneities in the BIAS structure, resulting in a more uniform frame that can be reliably subtracted from the SCIENCE images.

Flat-Field Correction

Flat-field frames quantify the pixel-to-pixel sensitivity of the detector. Even under uniform illumination, each pixel responds differently due to small variations in quantum efficiency or dust contamination in the optical path. To correct this, the telescope pupil was illuminated uniformly (for example, by the twilight sky), and multiple flat-field exposures were taken. Each FLAT frame was first debiased by subtracting $\tilde{B}$:

$$F_r = F - \tilde{B}$$

The propagated uncertainty per FLAT frame is:

$$\sigma_{F_r} = \sqrt{\mathrm{RON}^2 + \sigma_{\tilde{B}}^2 + \left|F - \tilde{B}\right|}$$

That is, the squared sum of: the RON reported in the header of the FLAT frames, the error associated with the median bias, and the photon noise due to the Poisson distribution of arriving photons, which is the square root of the signal.

A normalization factor f_{norm} was then computed for each frame by taking the median of a 50 × 50-pixel region near the center. Each debiased flat was divided by its corresponding normalization factor:

$$\widehat{F_r} = \frac{F_r}{f_{\mathrm{norm}}}$$

Finally, the median normalized flat $\widetilde{\widehat{F_r}}$ was obtained, with error propagation according to:

$$\sigma_{\widetilde{\widehat{F_r}}} = \frac{1}{N}\sqrt{\sum_{i=1}^{N}\left(\frac{\sigma_{F_{r_i}}}{\widetilde{f_{\mathrm{square}_i}}}\right)^2}$$

This produced a final median flat with all corrections applied, as seen in Figure 1, which illustrates the bias and flat-field calibration process. This produced a final median flat with all corrections applied.

Figure 1.

Calibration frames used in the data reduction process. Left: Example of a raw bias frame (top) and the resulting median-combined master bias (bottom). Right: Example of a raw flat-field frame (top) and its median-combined profile (bottom), showing the illumination gradient across the detector.

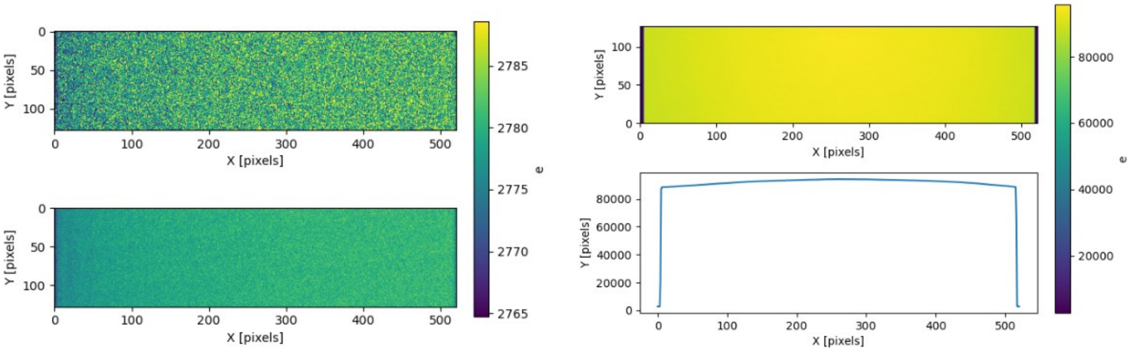

Science frames correction

Having generated the median BIAS and FLAT frames, we corrected the science frames. Each science frame S was first debiased as:

$$S_{\mathrm{db}} = S - \tilde{B}$$

with error:

$$\sigma_{S_{\mathrm{db}}} = \sqrt{\mathrm{RON}^2 + \sigma_{\tilde{B}}^2 + S_{\mathrm{db}}}$$

Then each $\boldsymbol{S}_{\mathrm{db}}$ frame was divided by the normalized median flat $\tilde{\tilde{F}}_r$ to obtain the corrected science frame as:

$$S_{\mathrm{cr}} = \frac{S_{\mathrm{d}}}{\tilde{\tilde{F}}_r}$$

And whose error propagation is given by

$$\sigma_{S_{\mathrm{corr}}} = S_{\mathrm{corr}} \sqrt{\left(\frac{\sigma_{S_{\mathrm{db}}}}{S_{\mathrm{db}}}\right)^2 + \left(\frac{\sigma_{\tilde{\tilde{F}}_r}}{\tilde{\tilde{F}}_r}\right)^2}$$

A time correction was also applied: each FITS timestamp in Julian Date (JD) was converted to Barycentric Julian Date (BJD) and then Barycentric Dynamical Time (TDB) to account for relativistic and positional effects using Astropy.

Photocenter computation

Next, the host star WASP-10 was identified by comparing one science frame with the SIMBAD catalogue (Wenger et al., 2000) at coordinates $23^h15^m58.33^s$ RA and +31°27′45.9″ DEC. After locating the target, its photocenter was computed as the flux-weighted centroid of its pixels. A circular aperture was defined around the star with a radius sufficient to contain its flux and some background; the average distance to the flux center was used to determine precise centroid coordinates.

A second larger ring defined an annulus used to estimate the median sky background ϕ_{sky} and its error:

$$\sigma_{\phi_{\text{sky}}} = \frac{1}{N}\sqrt{\sum \sigma^2_{S_{\text{corr}}}}$$

The sky background was then subtracted from the science frames:

$$S_{\text{sycr}} = S_{\text{cr}} - \phi_{\text{sky}}$$

with propagated error:

$$\sigma_{S_{\text{sky-corr}}} = \sqrt{\sigma^2_{\phi_{\text{sky}}} + \sigma^2_{S_{\text{corr}}}}$$

This procedure resulted in the final set of calibrated, sky-corrected science frames, as seen in Figure 2.

Figure 2.

Top: Sky field around WASP-10 obtained from the DSS survey and retrieved from SIMBAD, showing the TASTE observation frame (yellow dashed box) and the target star (red dashed circle). Bottom: Corresponding TASTE image of the same region, with the target star highlighted in red.

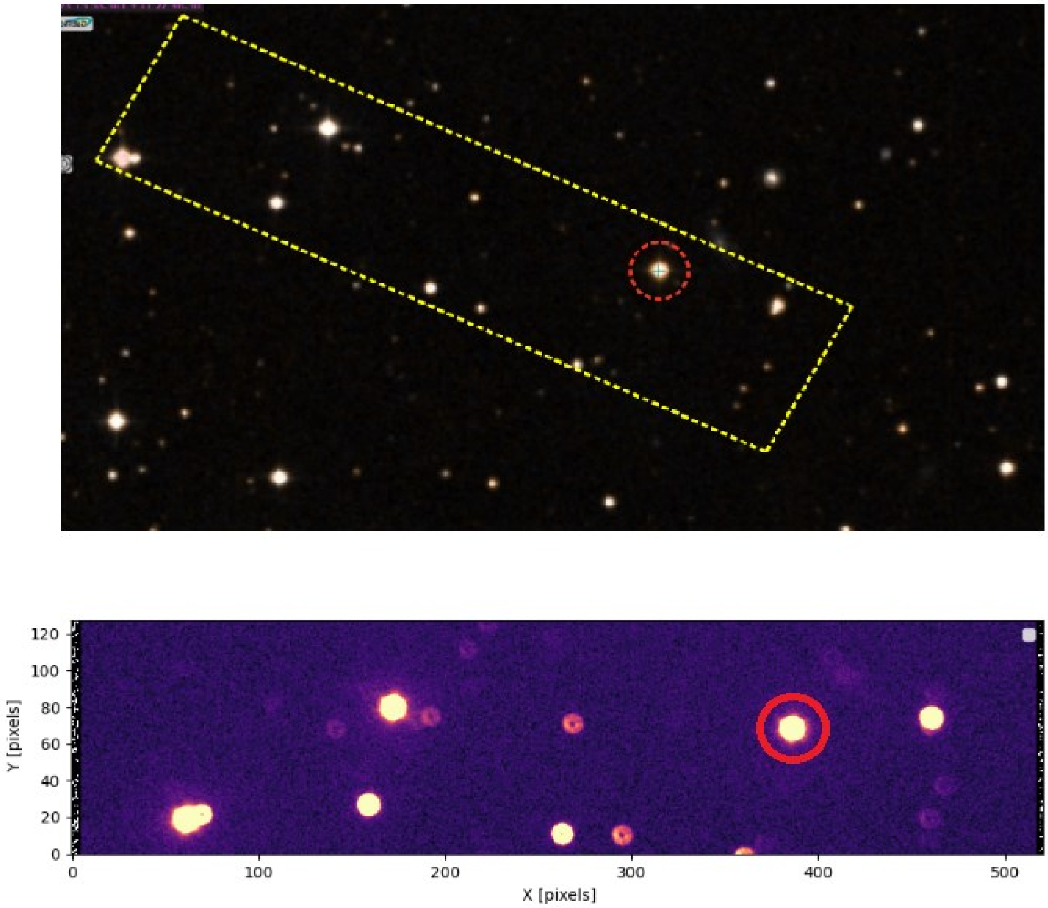

Aperture photometry

Since the Transit method consists on being able to detect a star's decrease in luminosity when a planet crosses in front of it, we must utilize a technique with which we can very precisely quantify and analyze the flux of the star across time as received on the CCD before, during and after the transit; to do so we perform aperture photometry.

Aperture photometry is a technique utilized to study the flux of photons emitted by a source across time as observed by the detector, a perimeter of pixels or "aperture" is selected in the science frame as a boundary, where the pixels that fall inside the aperture correspond to the ones where the the flux of the source is being measured across multiple frames, the perimeter can have different shapes, however in our case a radial symmetry, or ring was selected as the aperture.

The ring perimeter is a different one from the ones used for the photocenter calculation and the sky background subtraction as each serves different purposes, in the case of the aperture photometry, the aperture ring size is smaller than the previous cases, as our objective with aperture photometry is to quantify the change in flux on the pixels of the CCD which receive the photons from the source, the aperture size should only include flux from the source and not background sky and is centered on the computed photocenter of the studied source.
The total flux of the star φ_i and its associated uncertainty $\sigma\varphi_i$ for each timestamp were calculated as:

$$\phi_i = \sum_{d<R_{\text{ap}}} S_{\text{sky-corr}}$$

$$\sigma_{\phi_i} = \sqrt{\sum_{d<R_{\text{ap}}} \sigma^2_{S_{\text{sky-corr}_i}}}$$

Differential photometry
We must also take into account that the dip in the star's flux may be caused by phenomena unrelated to the planetary transit. To remove the influence of such effects in our data analysis, we performed differential photometry on the TASTE dataset.

In differential photometry ($\Delta\phi$), aperture photometry is carried out not only on the target star but also on one or more reference stars. The flux of the target is then compared to the combined flux of the reference stars across all frames. By doing so, we can track the target's brightness variations relative to the references over the same timestamps. Since the transit signal appears only in the target star, while other environmental effects such as atmospheric variations or instrumental drift affect all stars equally, this comparison allows us to remove first-order systematic trends. These include the influence of the Moon illuminating the sky, thin passing clouds, or changes in airmass during the observation. The process also helps to normalize the target's flux, producing a cleaner light curve.

Ideally, the chosen reference stars should have a brightness similar to that of the target and be located in regions of the CCD free from nearby sources that could contaminate their flux. The selection of reference stars was performed by adjusting the color scale of one of the SCIENCE frames, where the color scale represents the relative flux intensity across the image. We visually selected stars of comparable brightness to WASP-10, ensuring that their surroundings were free of contaminating flux. The target and selected reference stars on the science frame are shown in Figure 3.

Figure 3.

Identification of the target (WASP-10) and the three reference stars used for differential photometry. Each aperture is marked with a colored circle corresponding to its designation in the legend. The color scale represents the recorded flux in photoelectrons.

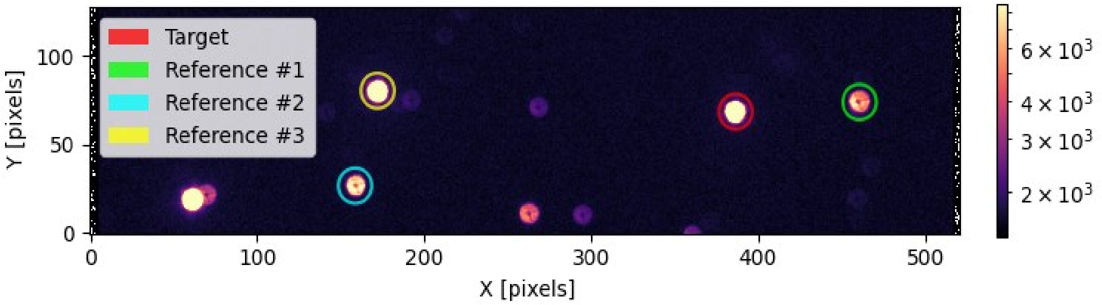

The size of the aperture used for the differential photometry was determined by plotting the flux of the target star in a distribution as a function of radius (the size of the aperture in pixels) where three aperture sizes were selected, those of 7, 8 and 9 pixels of radius, for a relative flux of 95%, 98% and 99% of the target's flux passing through each aperture size respectively seen here in Figure 4.

Figure 4.

Fractional flux enclosed within circular apertures of increasing radius. The vertical colored lines mark the fractional flux that falls inside different aperture values.

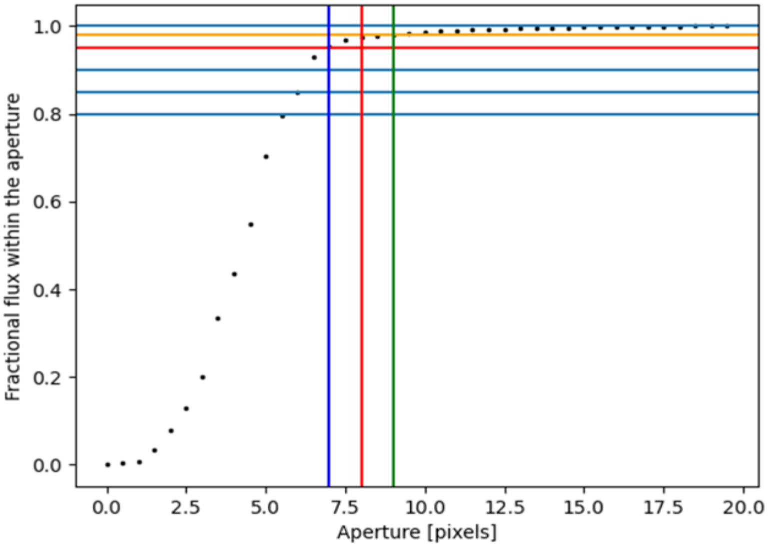

The differential photometry itself was computed by dividing the flux of a given aperture for the target star over the sum of the fluxes of the reference stars as:

The differential flux Δφ was then calculated as:

$$\Delta\phi = \frac{\phi_{target}}{(\phi_1 + \phi_2 + \phi_3)}$$

Where the combined uncertainty from target and reference stars was computed as:

$$\sigma_{\phi_{\mathrm{refs}}} = \sqrt{\sigma_{\phi_1}^2 + \sigma_{\phi_2}^2 + \sigma_{\phi_3}^2}$$

So the associated error of the differential photometry is therefore:

$$\sigma_{\Delta\phi} = \Delta\phi\sqrt{\left(\frac{\sigma_{\phi_{\mathrm{target}}}}{\phi_{\mathrm{target}}}\right)^2 + \left(\frac{\sigma_{\phi_{\mathrm{refs}}}}{\phi_1 + \phi_2 + \phi_3}\right)^2}$$

Multiple differential photometry runs were tested, varying aperture size and reference-star combinations; the best result corresponded to a 7-pixel aperture with all three reference stars, which yielded the smallest standard deviation as shown in figure 5.

Figure 5.

Aperture photometry masks for the target (WASP-10) and three reference stars. The magenta and cyan circles represent the inner and outer radii used to define the source and background annuli, respectively. The color scale indicates the recorded flux in photoelectrons

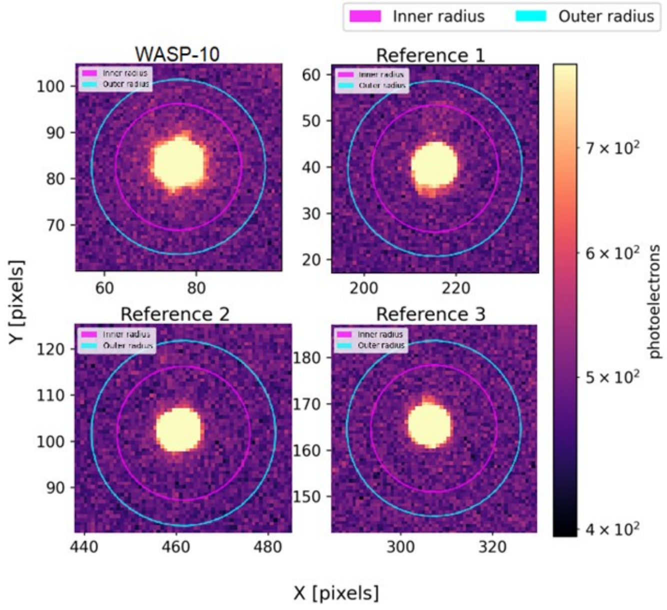

Finally, the differential fluxes were normalized by fitting a first-degree polynomial p_1 to the out-of-transit points and dividing the fluxes by p_1:

$$\widehat{\Delta\phi} = \frac{\Delta\phi}{p_1}$$

with propagated error:

$$\sigma_{\widehat{\Delta\phi}} = \frac{\sigma_{\Delta\phi}}{p_1}$$

The resulting normalized light curve, top panel on Figure 6, represents the transit of WASP-10b from the TASTE dataset.

The sky conditions during the night of observation for the transit on the TASTE dataset can be seen in three lower panels on Figure 6 as measured by the aperture photometry performed on each star.

Figure 6.

Photometric and observational parameters from the TASTE dataset. The first panel shows the normalized flux for the target and three reference stars. The second panel displays the evolution of airmass during the observation. The third panel shows the sky background level for each source, while the fourth panel presents the telescope drift in the X and Y directions.

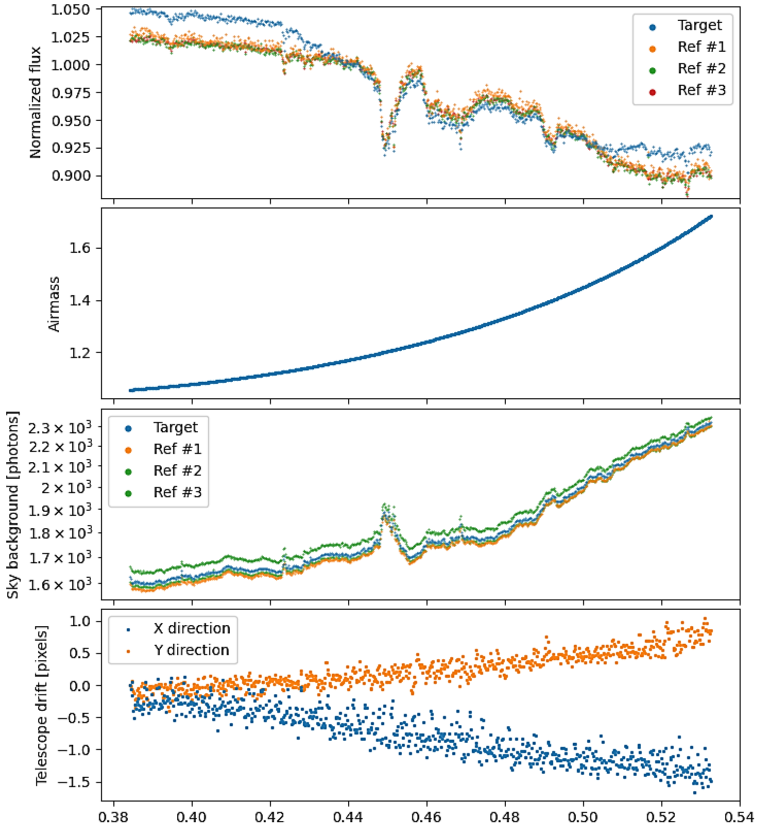

TESS Data Processing

For the TESS data reduction, Target Pixel Files (TPF) were used rather than Full-Frame Images (FFIs). These TPFs are small cutouts of the CCD that focus on a specific region of interest and include a precomputed light curve (LCF) derived from the same data. Both file types are provided in FITS format.

The dataset was downloaded from the Barbara A. Mikulski Archive for Space Telescopes (MAST). Some initial preprocessing had already been performed by the Science Processing Operations Center (SPOC) at NASA Ames Research Center. This included BIAS and FLAT corrections, background subtraction, time conversion to Barycentric Julian Date in Barycentric Dynamical Time (BJD TDB), Simple Aperture Photometry (SAP), and Pre-search Data Conditioning SAP (PDCSAP).

The SAP flux corresponds to the sum of the pixel values within a defined aperture, while PDCSAP further removes long-term instrumental trends using Co-trending Basis Vectors. Each observation is accompanied by a set of quality flags encoded as a bitmask in the FITS header, identifying conditions such as cosmic-ray events or data discontinuities (TESS Instrument Handbook).

Although TESS data are not affected by atmospheric interference, instrumental and orbital effects can still cause small variations in the recorded flux. To remove these residual trends, we applied a detrending procedure using the WOTAN library (Hippke et al., 2019). A Huber-spline fit was computed for the out-of-transit points, effectively flattening the baseline without introducing additional noise:

$$\sigma_{\text{TESS flattened}} = \frac{\sigma_{\text{TESS}}}{\text{TESS huberspline}}$$

Each flux measurement was then divided by its corresponding spline-fit value, producing a flattened light curve in which the planetary transits appear as distinct decreases in flux. A manual mask was applied to isolate the in-transit and out-of-transit regions, as shown in Figure 7.

Figure 7.
Light curves from TESS Sector 56 before and after flattening. The left panel shows the unflattened light curve with clear long-term trends, while the right panel displays the same data after flattening with the applied model (red line). Blue points represent the observations, and vertical bars show the measurement errors.

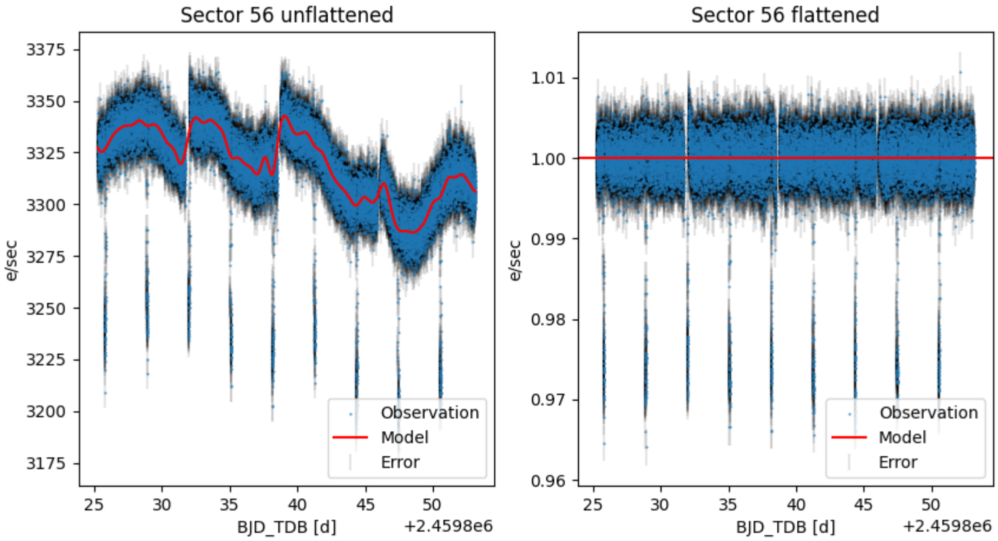

Limb Darkening

After completing the processing of both the TASTE and TESS datasets, a final correction was applied to the models to account for the limb darkening effect.

Limb darkening occurs because the temperature in a star's atmosphere decreases outward from the center. Light emitted near the stellar limb originates from cooler, shallower layers, making the edge of the stellar disk appear dimmer than the center. This effect must be included in transit modeling, as it influences the apparent fraction of stellar flux blocked by the planet depending on its transit path across the star.

To determine the limb-darkening coefficients, we used the Python Limb Darkening Toolkit (LDTk) (Parviainen & Aigrain, 2015). The toolkit interpolates stellar atmosphere models to estimate the coefficients from known stellar parameters and filter transmission curves.

For WASP-10, the adopted stellar parameters from the Exoplanet Follow-Up Observing Program (ExoFOP) were:

- Effective temperature T_{exe} = 4713.98 K
- Surface gravity log g = 4.5649
- Metallicity Z = 0.0428

The filter passbands were taken from the FITS headers:

- TASTE: r-Sloan
- TESS: SDSS r full transmission Filter transmission data were retrieved from the SVO Filter Profile Service (Rodrigo et al., 2012).

LDTk generated thousands of synthetic limb-darkening profiles per filter; their means were adopted as the coefficients, and their standard deviations as uncertainties.

With these coefficients, we modeled the transits using the BATMAN package (Kreidberg, 2015), which computes analytical light curves for arbitrary limb-darkening laws. BATMAN was used to extract planetary parameters from the TESS and TASTE light curves.

LIKELIHOOD OF MODEL AND FITTING

A Bayesian framework was employed to evaluate the model fit to the data. Bayesian inference combines the prior $P(x)$, representing previously known information, and the likelihood $\mathcal{L}(x)$, representing the probability of observing the data given a model, to produce the posterior probability $P(x \mid D)$:

$$P(\, x \mid D\,) = \frac{\mathcal{L}(x)\, P(x)}{P(D)}$$

Our transit model $m(\boldsymbol{\theta})$ depends on 14 parameters ($\theta_1 - \theta_{14}$), listed in Table 1, including the orbital parameters, limb-darkening coefficients for each filter, polynomial trend coefficients, and jitter terms.

The priors $P(\theta)$correspond to initial estimates of these parameters based on either:

- previously published literature values for WASP-10b (e.g., orbital period, inclination, semi-major axis, radius ratio).

- theoretical expectations (i.e., ranges of limb-darkening coefficients derived from stellar atmosphere models).

- fixed calibration parameters (e.g., polynomial coefficients for baseline normalization).

These priors define the initial parameter space that the algorithm explores, effectively constraining the model to physically reasonable values.

Assuming Gaussian uncertainties and uncorrelated data points, the likelihood function is expressed as

$$\mathcal{L}(\theta) \equiv P(\, y \mid \theta\,) = \prod_{i=1}^{N} \mathcal{L}_i = \prod_{i=1}^{N} \left(\frac{1}{\sqrt{2\pi}\,\sigma_i} \exp ! \left[- \frac{(y_i - m_i)^2}{2\sigma_i^2} \right] \right)$$

Simplifying via the chi-square sum:

$$\chi^2 = \sum_{i=1}^{N} \frac{(y_i - m_i)^2}{\sigma_i^2}$$

and taking logarithms:

$$\ln L = -\frac{1}{2} \left[N \ln(2\pi) + \chi^2 + \sum_{i=1}^{N} \ln(\sigma_i^2) \right]$$

The logarithmic prior depends on the limb-darkening parameters:

$$\ln P\,(\theta) = \ln u\,1_{\mathrm{TESS}} + \ln u\,2_{\mathrm{TESS}} + \ln u\,1_{\mathrm{TASTE}} + \ln u\,2_{\mathrm{TASTE}}$$

Finally, the posterior probability is:

$$\ln P\,(\,\theta \mid y\,) = \ln \mathcal{L} + \ln P\,(\theta) - \ln P\,(y)$$

Table 1.

Prior Parameters Used in the MCMC Sampler

θ	Parameter	Value	Units
θ_1	Inferior conjunction	2459825.800375 ± 0.000204	JD
θ_2	Orbital period	3.0927616 ± 0.0000112	days
θ_3	Scaled planet radius	0.15918 ± 0.00050	R_p / R★
θ_4	Scaled semi-major axis	11.65 ± 0.09	a / R★
θ_5	Orbital inclination	88.49 ± 0.22	deg
θ_{6-9}	Limb-darkening coefficients (TESS/TASTE)	see text	—
θ_{10-12}	Polynomial trend coefficients	—	—
θ_{13-14}	Jitter terms (TESS/TASTE)	—	—

MARKOV CHAIN MONTE CARLO (MCMC) SAMPLER

The logarithm of the posterior probability, ln $P(\theta|D)$, was sampled using a Markov-Chain-Monte-Carlo (MCMC) sampler (Foreman-Mackey et al., 2013). This sampler generates chains of uncorrelated random numbers, which we can use to pool independent samples for each of our parameters.

Given that we have known parameters θ, we can assume that there is a combination of them that maximizes the likelihood ln $\mathcal{L}$ of obtaining said values as results. The goal then was to find the set of parameters θ that maximizes the value of ln $\mathcal{L}$.

Thus, given that ln $\mathcal{L}$ and $P(\theta)$ both depend on θ, but $P(y)$ does not, ln $\mathcal{L}$ and $P(\theta)$ will both change with each new iteration of the sampler.

With the MCMC sampler, we generated 50 walkers over 20,000 steps in the 12 dimensions of our parameter space, plus 2 more parameters corresponding to corrective terms for both TESS and TASTE datasets, as seen in Figure 8. We also implemented the multiprocessing library (McKerns et al., 2012) to speed up the process by running various samplers simultaneously.

Figure 8.

Over the span of 20 000 iterations, the plot shows the parameter space traversed by the sampler as it converges for each parameter.

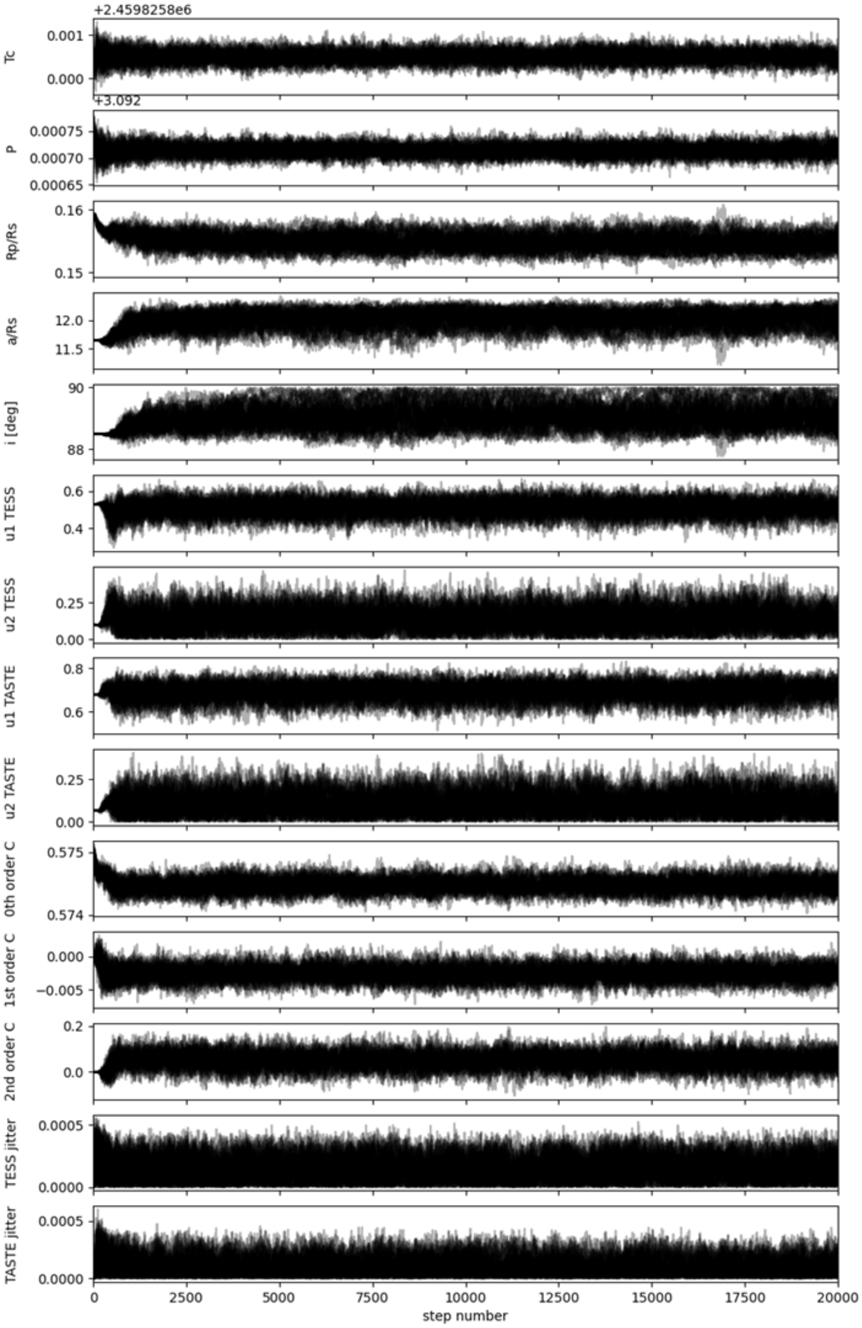

RESULTS

The MCMC sampling yielded posterior distributions for all model parameters, summarized in Table 2. These values represent the most probable estimates given the observational data and prior information. The joint and marginal posterior distributions are shown in Figure 9, where the shape of each contour indicates the degree of correlation between parameters. Elongated or skewed contours correspond to stronger correlations, while more circular contours suggest largely independent parameters.

Using the median values from the posterior distributions, we generated synthetic transit light curves for both the TESS and TASTE datasets. The resulting models, together with their residuals, are presented in Figure 10. The models show excellent agreement with the data, with residuals showing no significant structure, indicating that the adopted model accurately captures the observed transit profiles.

The correlations visible in the corner plot (Figure 9) are physically meaningful. For instance, the orbital inclination and scaled semi-major axis a, show a noticeable correlation with the planet-to-star radius ratio, $R_p/R_\star$. This relationship arises because variations in inclination change the planet's projected path across the stellar disk, altering the apparent transit depth due to limb darkening. Similarly, changes in the semi-major axis affect the transit duration, which in turn influences how the model constrains the planetary radius.

Overall, the recovered parameters are consistent with previously published values for WASP-10 b, confirming the reliability of our reduction and modeling procedure.

A quantitative comparison between the parameters derived in this work and those reported in previous studies is presented in Table 3, showing good agreement within the quoted uncertainties.

Figure 9.

Corner plot showing the relation between different parameters. Skewed contours indicate stronger correlations between the parameters involved, while more circular or homogeneous contours indicate weak or no correlation.

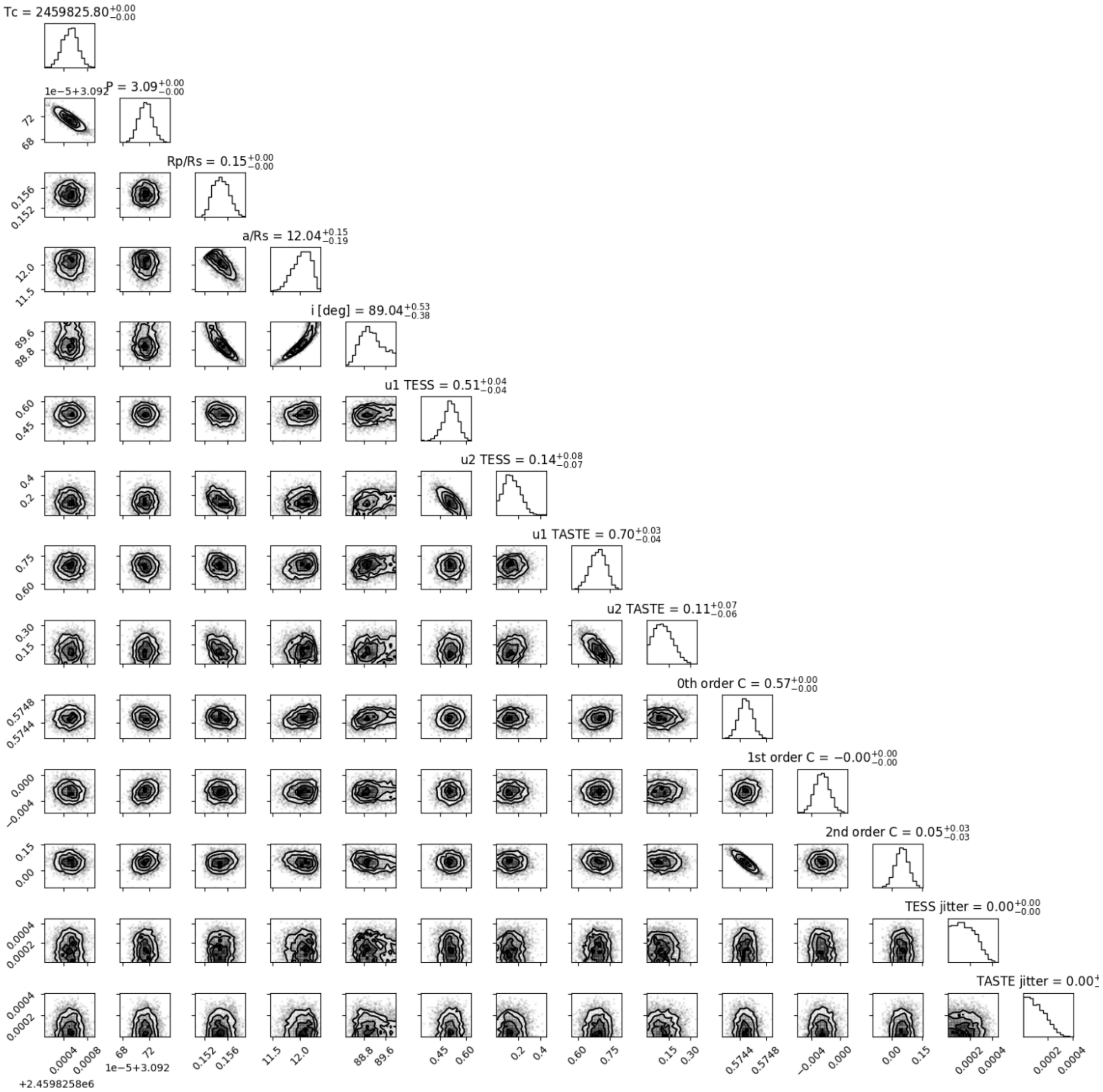

Table 2.

Posterior Parameter Estimates from the MCMC Analysis

$\theta_{\#}$	Parameter	Value	Units
θ_1	Inferior conjunction	2459685.39781 ± 0.00009	JD
θ_2	Orbital period	3.2130546 ± 0.0000008	days
θ_3	Scaled planet radius	0.1389 ± 0.0010	R_p / R★
θ_4	Scaled semi-major axis	11.38 ± 0.21	a / R★
θ_5	Orbital inclination	88.28 ± 0.30	deg
θ_{6-9}	Limb-darkening coefficients (TESS/TASTE)	see text	—
θ_{10-12}	Polynomial trend coefficients	—	—
θ_{13-14}	Jitter	—	—

Figure 10.

Final TESS and TASTE transit models derived from MCMC best-fit parameters, with residuals.

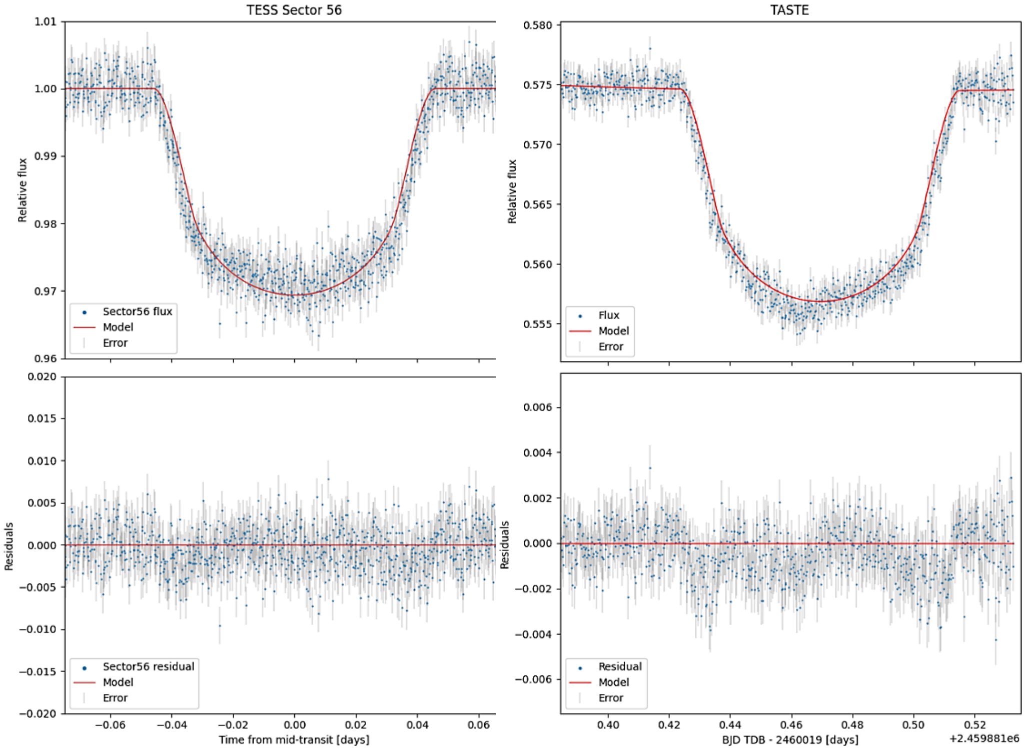

Table 3.
Comparison of Derived Parameters with Literature Parameters.

Source	Inferior Conjunction (JD)	Period (days)	R_p / R★	a / R★	i (deg)
Johnson et al. (2009)	2454664.03729 ± 0.00008	3.09276 ± 0.00001	0.1592 ± 0.0011	11.65 ± 0.13	88.49 ± 0.17
Sada et al. (2016)	2454664.03804 ± 0.00006	3.09273 ± 0.00000	0.1605 ± 0.0012	11.55 ± 0.18	88.26 ± 0.26
Kokori et al. (2023)	2456253.70052 ± 0.00008	3.09273 ± 0.00000	0.1592 ± 0.0011	11.65 ± 0.13	88.49 ± 0.22
This work	2459685.39781 ± 0.00009	3.21305 ± 0.00000	0.1389 ± 0.0010	11.38 ± 0.21	88.28 ± 0.30

DISCUSSION

The TASTE photometry presented significant challenges due to the intentional defocusing of the telescope, a technique used to prevent CCD saturation. This defocusing increased the required aperture size and made the selection of reference stars more sensitive to sky background variations, as seen in Figure 6. Despite these complications, stable flux ratios were achieved after several iterations of aperture and reference-star optimization, ensuring consistent differential photometry results.

The TESS observations, although limited to a single sector comprising nine transits, provided sufficient phase coverage to obtain a reliable orbital period for WASP-10 b. Acquiring data from additional sectors would allow for greater statistical robustness and tighter constraints on the derived planetary parameters.

The MCMC results are in good agreement with previously published values for WASP-10 b (Johnson et al. 2009; Sada et al. 2016; Kokori et al. 2023), as summarized in Table 3. This consistency confirms the validity of the reduction and modeling procedures applied to both datasets.

The correlations observed in the corner plot (Figure 9) are physically meaningful. Parameters such as the orbital inclination, semi-major axis, and scaled planet radius exhibit clear interdependencies. For instance, grazing transits with lower inclinations intersect the outer, dimmer stellar regions affected by limb darkening, resulting in shallower apparent transit depths. These relationships reinforce the physical consistency of the fitted parameters and validate the robustness of the MCMC modeling approach.

CONCLUSIONS

The combination of data from multiple surveys enhances the precision and reliability of derived exoplanetary parameters. Despite the differing observational conditions of ground-based (TASTE) and space-based (TESS) instruments, both datasets provide complementary information that strengthens the overall analysis.

The TESS observations supply multiple transits, enabling robust determination of the orbital period and global transit parameters, while the TASTE data capture atmospheric and instrumental effects present under terrestrial conditions. This combination allows cross-validation of the light-curve morphology and consistency of the extracted parameters between independent observing platforms.

The use of MCMC sampling proved especially valuable as a rigorous statistical framework, yielding posterior distributions that quantify both parameter uncertainties and correlations. This method provided a comprehensive assessment of the model's reliability and confirmed the physical consistency of the results.

Future work combining these datasets with spectroscopic and radial-velocity observations would enable tighter constraints on the planet's mass and could probe atmospheric composition, extending the analysis beyond the scope of the present study.

ACKNOWLEDGMENTS

Particular thanks go to the TASTE collaboration and the Department of Physics and Astronomy "Galileo Galilei" of the University of Padova for providing access to the ground-based observations obtained with the 1.82 m Copernico Telescope at the Asiago Astrophysical Observatory as part of the TASTE program. These data were made available for educational purposes. Appreciation is also extended to the Universidad de Panamá and the editorial board of *Tecnociencia* for supporting the dissemination of this work.

BIBLIOGRAPHIC REFERENCES

Astropy Collaboration, Price-Whelan, A.M., Lim, P.L., et al. (2022). The Astropy Project: Latest Major Release (v5.0) of the Core Package. *Astron. J.* 935(2): 167. https://doi.org/10.3847/1538-4357/ac7c74

Christian, D.J., Gibson, N.P., Simpson, E.K., et al. (2009). WASP-10 b: a 3 MJ gas-giant planet transiting a late-type K star. *Mon. Not. R. Astron. Soc.* 392(4): 1585–1590. https://doi.org/10.1111/j.1365-2966.2008.14164.x

Foreman-Mackey, D., Hogg, D.W., Lang, D. & Goodman, J. (2013). emcee: The MCMC Hammer. *Publ. Astron. Soc. Pac.* 125(925): 306–312. https://doi.org/10.1086/670067

Harris, C.R., Millman, K.J., van der Walt, S.J., et al. (2020). Array programming with NumPy. *Nature* 585(7825): 357–362. https://doi.org/10.1038/s41586-020-2649-2

Hippke, M., David, T.J., Mulders, G.D. & Heller, R. (2019). Wōtan: Comprehensive time-series detrending in Python. *Astron. J.* 158(4): 143. https://doi.org/10.3847/1538-3881/ab3984

Hunter, J.D. (2007). Matplotlib: A 2D graphics environment. *Comput. Sci. Eng.* 9(3): 90–95. https://doi.org/10.1109/MCSE.2007.55

Johnson, J.A., Winn, J.N., Cabrera, N.E. & Carter, J.A. (2009). A smaller radius for the transiting exoplanet WASP-10 b. *Astrophys. J.* 692(2): L100–L104. https://doi.org/10.1088/0004-637X/692/2/L100

Kokori, A., Tsiaras, A., Edwards, B., et al. (2023). ExoClock Project III: 450 new exoplanet ephemerides…. *Astrophys. J. Suppl. Ser.* 265(1): 4. https://doi.org/10.3847/1538-4365/ac9da4

Kreidberg, L. (2015). batman: Basic Transit Model Calculation in Python. *Publ. Astron. Soc. Pac.* 127(957): 1161–1165. https://doi.org/10.1086/683602

Mayor, M., & Queloz, D. (1995). A Jupiter-mass companion to a solar-type star. *Nature* 378(6555): 355–359. https://doi.org/10.1038/378355a0

McKerns, M.M., Strand, L., Sullivan, T., Fang, A., & Aivazis, M.A.G. (2012). Building a Framework for Predictive Science. *arXiv*:1202.1056. https://arxiv.org/abs/1202.1056

Nascimbeni, V., Piotto, G., Bedin, L.R., & Damasso, M. (2011). TASTE: Overview and improved parameters for HAT-P-3 b and HAT-P-14 b. *Astron. Astrophys.* 527: A85. https://doi.org/10.1051/0004-6361/201015199

TASTE Collaboration. (2022). *The Asiago Search for Transit Timing Variations of Exoplanets (TASTE).* Department of Physics and Astronomy "Galileo Galilei," University of Padova, Italy. Data provided by the TASTE team at the Asiago Astrophysical Observatory. Available at: https://groups.dfa.unipd.it/ESPG/taste.html (accessed 25 Oct 2025).

Parviainen, H., & Aigrain, S. (2015). LDTk: Limb Darkening Toolkit. *Mon. Not. R. Astron. Soc.* 453(4): 3821–3826. https://doi.org/10.1093/mnras/stv1857

Ricker, G.R., Winn, J.N., Vanderspek, R., et al. (2015). Transiting Exoplanet Survey Satellite (TESS). *J. Astron. Telesc. Instrum. Syst.* 1(1): 014003. https://doi.org/10.1117/1.JATIS.1.1.014003

Rodrigo, C., Solano, E., & Bayo, A. (2012). SVO Filter Profile Service, Version 1.0. *IVOA Working Draft,* 15 Oct 2012. https://doi.org/10.5479/ADS/bib/2012ivoa.rept.1015R

Sada, P.V., & Ramón-Fox, F.G. (2016). Exoplanet transits registered at the Universidad de Monterrey Observatory I. *Publ. Astron. Soc. Pac.* 128(960): 024402. https://doi.org/10.1088/1538-3873/128/960/024402

Wenger, M., Ochsenbein, F., Egret, D., et al. (2000). The SIMBAD astronomical database. *Astron. Astrophys. Suppl. Ser.* 143(1): 9–22. https://doi.org/10.1051/aas:2000332